Optimal and Numerical Solutions for an MHD Micropolar Nanofluid between Rotating Horizontal Parallel Plates

Sohail Nadeem[1], Sadaf Masood[1], Rashid Mehmood[1]*, Muhammad Adil Sadiq[2]

1 Department of Mathematics, Quaid-i-Azam University, 45320, Islamabad, 44000, Pakistan, **2** Dammam Community College, Department of Mathematics, KFUPM, Dharan, 31261, Saudi Arabia

* rmqau@hotmail.com

Abstract

The present analysis deals with flow and heat transfer aspects of a micropolar nanofluid between two horizontal parallel plates in a rotating system. The governing partial differential equations for momentum, energy, micro rotation and nano-particles concentration are presented. Similarity transformations are utilized to convert the system of partial differential equations into system of ordinary differential equations. The reduced equations are solved analytically with the help of optimal homotopy analysis method (OHAM). Analytical solutions for velocity, temperature, micro-rotation and concentration profiles are expressed graphically against various emerging physical parameters. Physical quantities of interest such as skin friction co-efficient, local heat and local mass fluxes are also computed both analytically and numerically through mid-point integration scheme. It is found that both the solutions are in excellent agreement. Local skin friction coefficient is found to be higher for the case of strong concentration i.e. n=0, as compared to the case of weak concentration n=0.50. Influence of strong and weak concentration on Nusselt and Sherwood number appear to be similar in a quantitative sense.

Introduction

The idea of micropolar fluid was introduced by Eringen [1–2]. This idea is a substantial generalization of the classical Navier Stokes model to discuss certain complex fluids. This particular class of fluids consists of rigid, randomly oriented spherical particles with microstructures such as liquid crystals, colloidal fluids, polymeric suspensions, hematological suspensions and animal blood etc. Extensive uses of micropolar fluid theory are given in the books of Lukaszewicz [3] and Eringen [4]. Bhargava et al [5] presented finite element solutions for mixed convective micropolar flow driven by a porous stretching sheet. Later on, Takhar et al [6] highlighted free convection MHD micropolar fluid flow between two porous vertical plates and perceived that velocity decreases with an increase in Hartman number. Stagnation point flow of a micropolar fluid towards a stretching sheet was investigated by Nazar et al [7]. Ziabakhsh et al [8] presented Homotopy analysis solutions of micropolar flow in a porous channel with heat and

mass transfer. Similarly, Ishak et al [9] considered magnetohydrodynamic flow of micropolar fluid towards a stagnation point on a vertical surface. Joneidi et al [10] inspected behavior of micropolar flow in a porous channel with high mass transfer. Influence of chemical reaction and thermal radiation on MHD micropolar flow over a vertical moving porous plate in a porous medium with heat generation was discussed by Mohamed et al [11] who found that the translational velocity across the boundary layer and the magnitude of micro rotation at the wall decreased with an increase in magnetic field and Prandtl number. Some noteworthy studies on micropolar fluids with certain physical constraints can be found in [12–16].

In the last few decades nanofluids have proved to be extremely promising heat transfer agents in modern day industry and in numerous engineering applications of global interest like biomedical, optical and electronic fields. Choi [17] initiated the astonishing idea of nanofluids. Later numerous researchers and scientists investigated various real life flow problems under the influence of nanofluids. Buongiorno [18] presented a novel study on describing flow and heat transfer mechanisms of nanofluids. Similarly Nield et al [19] discussed natural convective boundary-layer flow of a nanofluid past a vertical plate and observed that the reduced Nusselt number is a decreasing function of thermophoresis and Brownian motion parameter. Nadeem et al [20] presented the optimized analytical solution for oblique flow of a Casson nanofluid with convective boundary conditions. They found that nanoparticle concentration is an increasing function of stretching parameter and Brownian motion while it is a decreasing function of thermophoresis, Biot number and non-Newtonian (Casson) parameter. Ganji et al [21] conducted a valuable study on heat transfer of Cu-Water nanofluid flow between parallel plates and concluded that heat flux at the surface has a direct relationship with nanoparticle volume fraction. Ganji et al [22] discussed simulation of MHD Cuo-Water nanofluid flow and convective heat transfer under the influence of Lorentz forces. Some notable studies on the topic can be found in [23–41].

The main goal of the present study is to discuss hydromagnetic flow of a micropolar nanofluid between parallel plates. Optimal homotopy analysis method proposed by Liao [24–25] is utilized to obtain graphical results against embedding physical parameters. Numerical values for skin friction, Nusselt and Sherwood numbers are obtained through OHAM and also numerically through mid-point integration scheme [26–27]. It would be obligatory to mention that mid-point integration scheme is used to verify our obtained analytical results. It is found that both the results are in a very good agreement with each other.

Mathematical Formulation

Consider steady incompressible 3D flow of an electrically conducting micropolar nanofluid between two horizontal parallel plates. Both the fluid and the plates rotate together around the *y-axis* with a constant angular velocity Ω. The x and y − axes are taken along and perpendicular to the plate respectively while the z − axis is taken normal to the xy plane. The plates are placed at $y = 0$ and $y = h$. The lower plate is being stretched by two equal and opposite forces so that the position of the point (0,0,0) remains unchanged. A uniform magnetic flux with density B_0 acts along the y-axis. The upper plate is subject to constant wall suction velocity $v_0 (< 0)$ or constant wall injection velocity $v_0 (> 0)$ respectively as shown in Fig 1.

The governing equations of the flow problem can be stated as [5–11, 18]

$$\frac{\partial u}{\partial x} + \frac{\partial v}{\partial y} = 0, \tag{1}$$

$$u\frac{\partial u}{\partial x} + v\frac{\partial u}{\partial y} + 2\Omega w = -\frac{1}{\rho}\frac{\partial p}{\partial x} + \left(v + \frac{k_1^*}{\rho}\right)\nabla^2 u + \frac{k_1^*}{\rho}\frac{\partial N}{\partial y} - \frac{\sigma}{\rho}B_0^2 u, \tag{2}$$
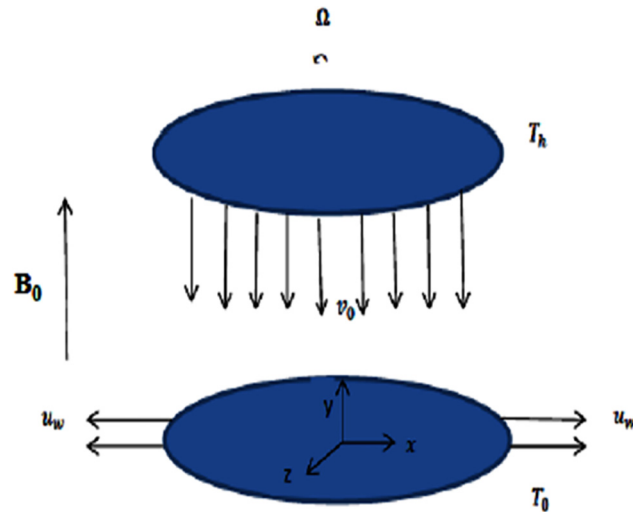
Fig 1. Physical description of the problem.

$$u\frac{\partial v}{\partial x} + v\frac{\partial v}{\partial y} = -\frac{1}{\rho}\frac{\partial p}{\partial y} + \left(v + \frac{k_1^*}{\rho}\right)\nabla^2 v + \frac{k_1^*}{\rho}\frac{\partial N}{\partial x},$$ (3)

$$u\frac{\partial w}{\partial x} + v\frac{\partial w}{\partial y} - 2\Omega u = \left(v + \frac{k_1^*}{\rho}\right)\nabla^2 w - \frac{\sigma}{\rho}B_0^2 w,$$ (4)

$$u\frac{\partial T}{\partial x} + v\frac{\partial T}{\partial y} = \frac{k}{\rho C_p}\nabla^2 T + \tau(D_B\nabla C.\nabla T + \frac{D_T}{T_\infty}\nabla T.\nabla T),$$ (5)

$$u\frac{\partial N}{\partial x} + v\frac{\partial N}{\partial y} = \frac{\gamma}{\rho j}\nabla^2 N - \frac{2k_1^*}{\rho j}N + \frac{k_1^*}{\rho j}\left(\frac{\partial v}{\partial x} - \frac{\partial u}{\partial y}\right),$$ (6)

$$u\frac{\partial C}{\partial x} + v\frac{\partial C}{\partial y} = D_B\nabla^2 C + \frac{D_T}{T_\infty}\nabla^2 T.$$ (7)

The appropriate boundary conditions are

$$u = ax, v = 0, w = 0, T = T_0, N = -n\frac{\partial u}{\partial y}, C = C_0 \ at \ y = 0,$$

$$u = 0, v = v_0, w = 0, T = T_h, N = n\frac{\partial u}{\partial y}, C = C_h \ at \ y = h,$$ (8)

where u, v and w are the velocity components along the x, y, z — directions respectively while $u = ax$ shows that lower plate is stretching.ρ is the density, ϑ is the kinematic viscosity, k_1^* is the vortex viscosity, N is the micro rotation velocity, Ω is the rotation velocity, B_0 is the magnetic field, σ is electrical conductivity, α is thermal diffusivity, k is the thermal conductivity, C_p is the specific heat of the fluid, j is the micro-inertia density, v_0 is the suction/injection velocity, T is the temperature of the fluid, T_0 is the temperature at lower plate, T_h is the temperature at upper plate. D_B Brownian diffusion coefficient, D_T is the thermophoresis diffusion coefficient, C is the

concentration and n is the boundary parameter. The case $n = 0$ represents strong concentration, $n = 0.5$ indicates weak concentration and vanishing of the antisymmetric part of the stress tensor and $n = 1$ represents turbulent flow. Spin gradient viscosity γ is defined as $\gamma = \left(\mu + \frac{k_1^*}{2}\right)j$.

Using transformations

$$
\left.\begin{array}{l}
u = axf'(\eta), \, v = -ahf(\eta), \, w = axg(\eta), \\
N = \dfrac{axG(\eta)}{h}, \theta(\eta) = \dfrac{T - T_h}{T_0 - T_h}, \, \varphi(\eta) = \dfrac{C - C_h}{C_0 - C_h}, \, \eta = \dfrac{y}{h}
\end{array}\right\} .
\tag{9}
$$

Eq ([1](#)) is identically satisfied while Eqs. ([2](#))–([7](#)), in dimensionless form are given by

$$
(1 + N_1)f^{iv} - R(f'f'' - ff''') + N_1 G'' - Mf'' - 2Krg' = 0,
\tag{10}
$$

$$
(1 + N_1)g'' + R(fg' - gf') - Mg + 2Krf' = 0,
\tag{11}
$$

$$
\theta'' + Pr(Rf\theta' + N_b\theta'\phi' + N_t\theta'^2) = 0,
\tag{12}
$$

$$
N_2 G'' - N_1(2G + f'') - N_3 R(f'G - G'f) = 0,
\tag{13}
$$

$$
\phi'' + R.Scf\phi' + \frac{N_t}{N_b}\theta'' = 0,
\tag{14}
$$

with boundary conditions

$$
\begin{array}{l}
f(0) = 0, f'(0) = 1, g(0) = 0, \theta(0) = 1, G(0) = -nf''(0), \phi(0) = 1, \\
f(1) = \lambda, f'(1) = 0, \, g(1) = 0, \, \theta(1) = 0, G(1) = nf''(1), \, \phi(\infty) = 0,
\end{array}
\tag{15}
$$

where primes denote differentiation with respect to η. N_1 is the coupling parameter, N_2 is the spin-gradient viscosity parameter, R is the Reynold number, M is the magnetic parameter, Kr is the rotation parameter, Pr is the Prandtl number, Sc is the Schmidt number, N_b is the Brownian motion parameter and N_t is the thermophoresis parameter which are defined by

$$
\begin{array}{l}
N_1 = \dfrac{k_1^*}{\mu}, N_2 = \dfrac{v_s}{vh^2}, N_3 = \dfrac{j}{h^2}, R = \dfrac{ah^2}{v}, M = \dfrac{\sigma h^2 B_0^2}{\rho v}, Kr = \dfrac{h^2\Omega}{v}, Pr = \dfrac{\mu C_p}{k}, \\
\tau = \dfrac{(\rho C_p)_{nf}}{(\rho C_p)_f}, N_t = \dfrac{\tau D_T(T_0 - T_h)}{vT_\infty}, N_b = \dfrac{\tau D_B(C_0 - C_h)}{v}, Sc = \dfrac{v}{D_B}, \lambda = -\dfrac{v_0}{h}.
\end{array}
\tag{16}
$$

The skin friction coefficient C_f, Nusselt number Nu and Sherwood number Sh are defined as

$$
C_f = \frac{\tau_w}{\rho u_w^2}, Nu = \frac{hq_w}{k(T_0 - T_h)}, Sh = \frac{hj_w}{D_B(C_0 - C_h)},
\tag{17}
$$

where

$$
\tau_w = \left(\left(\mu + k_1^*\right)\frac{\partial u}{\partial y} + k_1^* N\right)_{y=0}, q_w = -k\left(\frac{\partial T}{\partial y}\right)_{y=0}, j_w = -D_B\left(\frac{\partial C}{\partial y}\right)_{y=0}.
\tag{18}
$$

The dimensionless forms of skin friction coefficient $\dot{C}_f$, Nusselt number Nu and Sherwood

number Sh are

$$C_f^{'} = (1 + N_1)f^{''}(0) + N_1 G(0), Nu = -\theta^{'}(0), Sh = -\phi^{'}(0). \qquad (19)$$

Method of Solution

1. Optimal HAM Solution

The governing system of coupled ordinary differential Eqs (10)–(14) is nonlinear and extremely complicated in nature. These equations are solved analytically by optimal homotopy analysis method (OHAM). Following Liao [24–25] we know that $f(\eta), g(\eta), \theta(\eta), G(\eta)$ and $\phi(\eta)$ can be expressed by a set of a certain type of exponential base functions

$$\{\eta^k \exp(-m\eta)\,|k \geq 0, m \geq 0\}, \qquad (20)$$

in the forms

$$f(\eta) = a_{0,0}^0 + \sum_{m=0}^{\infty}\sum_{k=0}^{\infty} a_{n,m}^k y^k \exp(-my), \qquad (21)$$

$$g(\eta) = \sum_{m=0}^{\infty}\sum_{k=0}^{\infty} b_{n,m}^k y^k \exp(-my), \qquad (22)$$

$$\theta(\eta) = \sum_{m=0}^{\infty}\sum_{k=0}^{\infty} c_{n,m}^k y^k \exp(-my), \qquad (23)$$

$$G(\eta) = \sum_{m=0}^{\infty}\sum_{k=0}^{\infty} d_{n,m}^k y^k \exp(-my), \qquad (24)$$

$$\phi(\eta) = \sum_{m=0}^{\infty}\sum_{k=0}^{\infty} e_{n,m}^k y^k \exp(-my), \qquad (25)$$

in which $a_{m,n}^k, b_{m,n}^k, c_{m,n}^k, d_{m,n}^k$ and $e_{m,n}^k$ are series coefficients. The initial guesses f_0, g_0, θ_0, G_0 and ϕ_0 for $f(\eta), g(\eta), \theta(\eta), G(\eta)$ and $\phi(\eta)$ are selected as follows

$$f_0(\eta) = (1 - 2\lambda)\eta^3 + (3 - 2\lambda)\eta^2 + \eta, \qquad (26)$$

$$g_0(\eta) = 0, \qquad (27)$$

$$\theta_0(\eta) = 1 - \eta, \qquad (28)$$

$$G_0(\eta) = -n(6\lambda - 4 + 2\eta), \qquad (29)$$

$$\phi_0(\eta) = 1 - \eta. \qquad (30)$$

We select the auxiliary linear operators as

$$L_f = \frac{d^4 f}{d\eta^4}, L_g = \frac{d^2 g}{d\eta^2}, L_\theta = \frac{d^2 \theta}{d\eta^2}, L_G = \frac{d^2 G}{d\eta^2}, L_\phi = \frac{d^2 \phi}{d\eta^2}\Bigg\}. \qquad (31)$$

The above linear operators have the following properties

$$L_f\{C_0 + C_1\eta + C_2\eta^2 + C_3\eta^3\} = 0, \qquad (32)$$

$$L_g\{C_4 + C_5\eta\} = 0, \qquad (33)$$

$$L_\theta \{C_6 + C_7 \eta\} = 0, \tag{34}$$

$$L_G \{C_8 + C_9 \eta\} = 0, \tag{35}$$

$$L_\phi \{C_{10} + C_{11} \eta\} = 0, \tag{36}$$

Where $C_0 - C_{11}$ are arbitrary constants.

The zeroth order homotopic deformation equations can be written as

$$(1-p)L_f \{\hat{f}(\eta; p) - f_0(\eta)\} = p c_0^f N_f(\hat{f}(\eta; p), \hat{g}(\eta; p), \hat{G}(\eta; p)), \tag{37}$$

$$(1-p)L_g \{\hat{g}(\eta; p) - g_0(\eta)\} = p c_0^g N_g(\hat{f}(\eta; p), \hat{g}(\eta; p)), \tag{38}$$

$$(1-p)L_\theta \{\hat{\theta}(\eta; p) - \theta_0(\eta)\} = p c_0^\theta N_\theta(\hat{f}(\eta; p), \hat{\theta}(\eta; p), \hat{\phi}(\eta; p)), \tag{39}$$

$$(1-p)L_G \{\hat{G}(\eta; p) - G_0(\eta)\} = p c_0^G N_G(\hat{f}(\eta; p), \hat{G}(\eta; p)), \tag{40}$$

$$(1-p)L_\phi \{\hat{\phi}(\eta; p) - \phi_0(\eta)\} = p c_0^\phi N_\phi(\hat{f}(\eta; p), \hat{\theta}(\eta; p), \hat{\phi}(\eta; p)), \tag{41}$$

$$\hat{f}(0; p) = 0, \hat{f}'(0; p) = 0, \hat{g}(0; p) = 0, \hat{\theta}(0; p) = 0, \hat{G}(0; p) = -n\hat{f}''(0; p), \hat{\phi}(0; p) = 0, \tag{42}$$

$$\hat{f}(1; p) = 0, \hat{f}'(1; p) = 0, \hat{g}(1; p) = 0, \hat{\theta}(1; p) = 0, \hat{G}(0; p) = n\hat{f}''(0; p), \hat{\phi}(1; p) = 0, \tag{43}$$

where $p \; \epsilon \; [0, 1]$ indicates the embedding parameter and c_0^f, c_0^g, c_0^θ, c_0^G and c_0^ϕ the nonzero auxiliary parameters. Moreover the nonlinear operators N_f, N_g, N_θ, N_G and N_ϕ are prescribed as

$$N_f(\hat{f}(\eta; p), \hat{g}(\eta; p), \hat{G}(\eta; p))$$
$$= (1 + N_1)\frac{\partial^4 \hat{f}(\eta; p)}{\partial \eta^4} - R\left(\frac{\partial \hat{f}(\eta; p)}{\partial \eta}\frac{\partial^2 \hat{f}(\eta; p)}{\partial \eta^2} - \hat{f}(\eta; p)\frac{\partial^3 \hat{f}(\eta; p)}{\partial \eta^3}\right) + N_1 \frac{\partial^2 \hat{G}(\eta; p)}{\partial \eta^2}$$
$$- M\frac{\partial^2 \hat{f}(\eta; p)}{\partial \eta^2} - 2Kr\frac{\partial \hat{g}(\eta; p)}{\partial \eta}, \tag{44}$$

$$N_g\big(\hat{f}(\eta;p),\hat{g}(\eta;p)\big)$$

$$= (1+N_1)\frac{\partial^2 \hat{g}(y;p)}{\partial \eta^2} + R\left(\hat{f}(\eta;p)\frac{\partial \hat{g}(\eta;p)}{\partial \eta} - \hat{g}(\eta;p)\frac{\partial \hat{f}(\eta;p)}{\partial \eta}\right) - M\hat{g}(\eta;p)$$

$$+ 2Kr\frac{\partial \hat{f}(\eta;p)}{\partial \eta}, \tag{45}$$

$$N_\theta\big(\hat{f}(\eta;p),\hat{\theta}(\eta;p),\hat{\phi}(\eta;p)\big)$$

$$= \frac{\partial^2 \hat{\theta}(y;p)}{\partial \eta^2} + Pr\left(R\hat{f}(\eta;p)\frac{\partial \hat{\theta}(y;p)}{\partial \eta} + N_b\frac{\partial \hat{\theta}(y;p)}{\partial \eta}\frac{\partial \hat{\phi}(y;p)}{\partial \eta} + N_t\left(\frac{\partial \hat{\theta}(y;p)}{\partial \eta}\right)^2\right), \tag{46}$$

$$N_G\big(\hat{f}(\eta;p),\hat{G}(\eta;p)\big)$$

$$= N_2\frac{\partial^2 \hat{g}(y;p)}{\partial \eta^2} - N_1\left(2\hat{G}(\eta;p) + \frac{\partial^2 \hat{f}(\eta;p)}{\partial \eta^2}\right)$$

$$- N_3R\left(\frac{\partial \hat{f}(\eta;p)}{\partial \eta}\hat{g}(\eta;p) - \frac{\partial \hat{g}(\eta;p)}{\partial \eta}\hat{f}(\eta;p)\right)+, \tag{47}$$

$$N_\phi\big(\hat{f}(\eta;p),\hat{\theta}(\eta;p),\hat{\phi}(\eta;p)\big) = \frac{\partial^2 \hat{\phi}(y;p)}{\partial y^2} + R.Sc\hat{f}(y;p)\frac{\partial \hat{\phi}(y;p)}{\partial y} + \frac{N_t}{N_b}\frac{\partial^2 \hat{\theta}(y;p)}{\partial y^2}. \tag{48}$$

When p varies from 0 to 1, we have

$$\left.\begin{array}{l} \hat{f}(\eta;0) = f_0(\eta), \hat{f}(\eta;1) = f(\eta), \\ \hat{g}(\eta;0) = g_0(\eta), \hat{g}(\eta;1) = g(\eta), \\ \hat{\theta}(\eta;0) = \theta_0(\eta), \hat{\theta}(\eta;1) = \theta(\eta), \\ \hat{G}(\eta;0) = G_0(\eta), \hat{G}(\eta;1) = G(\eta), \\ \hat{\phi}(\eta;0) = \phi_0(\eta), \hat{\phi}(\eta;1) = \phi(\eta), \end{array}\right\}. \tag{49}$$

By means of Taylor's series

$$f_m(\eta) = \frac{1}{m!}\frac{\hat{f}(\eta;p)}{\partial \eta^m}\Bigg|_{p=0}, g_m(\eta) = \frac{1}{m!}\frac{\hat{g}(\eta;p)}{\partial \eta^m}\Bigg|_{p=0}, G_m(\eta) = \frac{1}{m!}\frac{\hat{G}(\eta;p)}{\partial \eta^m}\Bigg|_{p=0},$$

$$\theta_m(\eta) = \frac{1}{m!}\frac{\hat{\theta}(\eta;p)}{\partial \eta^m}\Bigg|_{p=0}, \phi_m(\eta) = \frac{1}{m!}\frac{\hat{\phi}(y;p)}{\partial y^m}\Bigg|_{p=0}. \tag{50}$$

The auxiliary converging parameters are chosen in such a way that the series (50) converges

when $p = 1$. Thus we have

$$f(\eta) = f_0(\eta) + \sum_{m=1}^{\infty} f_m(\eta), \tag{51}$$

$$g(\eta) = g_0(\eta) + \sum_{m=1}^{\infty} g_m(\eta), \tag{52}$$

$$\theta(\eta) = \theta_0(\eta) + \sum_{m=1}^{\infty} \theta_m(\eta), \tag{53}$$

$$G(\eta) = G_0(\eta) + \sum_{m=1}^{\infty} G_m(\eta), \tag{54}$$

$$\phi(\eta) = \phi_0(\eta) + \sum_{m=1}^{\infty} \phi_m(\eta). \tag{55}$$

The resulting $mth - order$ deformation equations are

$$L_f\{f_m(\eta) - \chi_{m-1} f_{m-1}(\eta)\} = c_0^f R_m^f(\eta), \tag{56}$$

$$L_g\{g_m(\eta) - \chi_{m-1} g_{m-1}(\eta)\} = c_0^g R_m^g(\eta), \tag{57}$$

$$L_\theta\{\theta_m(\eta) - \chi_{m-1} \theta_{m-1}(\eta)\} = c_0^\theta R_m^\theta(\eta), \tag{58}$$

$$L_G\{G_m(\eta) - \chi_{m-1} G_{m-1}(\eta)\} = c_0^G R_m^G(\eta), \tag{59}$$

$$L_\phi\{\phi_m(\eta) - \chi_{m-1} \phi_{m-1}(\eta)\} = c_0^\phi R_m^\phi(\eta), \tag{60}$$

$$f_m(0) = 0, \ f_m(1) = 0, \ f'_m(0) = 0, \ f'_m(1) = 0, \ G_m(0) = -nf''_m(0), \ g_m(0) = 0, \ g_m(1)$$
$$= 0, \ \theta_m(0) = 0, \ \theta_m(1) = 0, \ G_m(0) = nf''_m(0), \ \phi_m(0) = 0, \ \phi_m(1) = 0, \tag{61}$$

with the following definitions

$$R_m^f(\eta) = (1 + N_1)f^{iv}_{m-1} - R\left(\sum_{k=0}^{m-1} f'_k f''_{m-1-k} - \sum_{k=0}^{m-1} f_k f'''_{m-1-k}\right) + N_1 g''_{m-1} - Mf''_{m-1}$$
$$- 2Krg'_{m-1}, \tag{62}$$

$$R_m^g(\eta) = (1 + N_1)g''_{m-1} + R\left(\sum_{k=0}^{m-1} f_k g'_{m-1-k} - \sum_{k=0}^{m-1} g_k f'_{m-1-k}\right) - Mg_{m-1} + 2Krf'_{m-1}, \tag{63}$$

$$R_m^\theta(\eta) = \theta''_{m-1} + Pr\left(R\sum_{k=0}^{m-1} f_k \theta'_{m-1-k} + Nb\sum_{k=0}^{m-1} \theta'_k \phi'_{m-1-k} + Nt\sum_{k=0}^{m-1} \theta'_k \theta'_{m-1-k}\right), \tag{64}$$

$$R_m^G(\eta) = N_2 G''_{m-1} - N_1(2G_{m-1} + f''_{m-1}) - N_3 R\left(\sum_{k=0}^{m-1} f'_k G_{m-1-k} \sum_{k=0}^{m-1} G'_k f_{m-1-k}\right), \tag{65}$$

$$R_m^\phi(\eta) = \phi''_{m-1} + Sc.R\sum_{k=0}^{m-1} f_k \phi'_{m-1-k} + \frac{Nt}{Nb}\theta''_{m-1}, \tag{66}$$

Table 1. Optimal convergence control parameters and total averaged squared residual errors using BVPh2. 0 when $N_1 = N_2 = N_3 = 0.10$, R = 0.20, n = 0.50, M = 0.10 = Kr = Nt = Nb = λ, Pr = 1 = Sc.

m	c_0^f	c_0^g	c_0^θ	c_0^G	c_0^ϕ	E_m^t	CPU TIME[S]
2.0	−0.79	−0.74	−1.06	−7.47	−0.83	5.86×10^{-3}	3.88
4.0	−0.87	−0.76	−1.10	−8.16	−0.89	4.78×10^{-6}	116.0
6.0	−0.89	−0.88	−0.91	−8.28	−1.08	1.67×10^{-9}	2453

doi:10.1371/journal.pone.0124016.t001

in which

$$\chi_m = \begin{cases} 0, m \leq 1 \\ 1, m > 1 \end{cases}. \tag{67}$$

The general solutions of Eqs (56)–(60) can be written as

$$f_m(\eta) = f_m^*(\eta) + C_0 + C_1\eta + C_2\eta^2 + C_3\eta^3, \tag{68}$$

$$g_m(\eta) = g_m^*(\eta) + C_4 + C_5\eta, \tag{69}$$

$$\theta_m(\eta) = \theta_m^*(\eta) + C_6 + C_7\eta, \tag{70}$$

$$G_m(\eta) = G_m^*(\eta) + C_8 + C_9\eta, \tag{71}$$

$$\phi_m(\eta) = \phi_m^*(\eta) + C_{10} + C_{11}\eta, \tag{72}$$

in which $f_m^*(y), g_m^*(y), \theta_m^*(y), G_m^*(y)$ and $\phi_m^*(y)$ are the particular solutions of the Eqs (68)–(72) Note that Eqs (56)–(60) can be solved by Mathematica one after the other in the order $m = 1,2,3, \cdots$

Optimal convergence-control parameters. We know that the homotopic series solutions involve the non-zero auxiliary parameters $c_0^f, c_0^g, c_0^\theta, c_0^G$ and c_0^ϕ which define the convergence-region of the Homotopy series solutions. To determine the optimal values of $c_0^f, c_0^g, c_0^\theta, c_0^G$ and c_0^ϕ we utilize the concept of minimization by defining the average squared residual errors as introduced by [24].

$$E_m^f = \frac{1}{k+1} \sum_{j=0}^{k} \{N_f(\sum_{i=0}^{m}\hat{f}(\eta), \sum_{i=0}^{m}\hat{g}(\eta), \sum_{i=0}^{m}\hat{G}(\eta))_{\eta=j\delta\eta}\}^2 d\eta, \tag{73}$$

$$E_m^g = \frac{1}{k+1} \sum_{j=0}^{k} \{N_g(\sum_{i=0}^{m}\hat{f}(\eta), \sum_{i=0}^{m}\hat{g}(\eta))_{\eta=j\delta\eta}\}^2 d\eta, \tag{74}$$

Table 2. Individual Averaged squared residual errors using optimal values at $m = 6$ from Table 1.

m	E_m^f	E_m^g	E_m^θ	E_m^G	E_m^ϕ	CPUTIME[S]
4.0	1.04×10^{-5}	1.17×10^{-8}	3.50×10^{-9}	6.18×10^{-8}	1.30×10^{-7}	2.12
6.0	1.59×10^{-9}	1.05×10^{-12}	1.13×10^{-12}	3.80×10^{-11}	3.96×10^{-11}	3.98
10	7.40×10^{-16}	2.38×10^{-20}	1.46×10^{-19}	2.39×10^{-17}	4.57×10^{-18}	8.69
14	4.85×10^{-22}	3.44×10^{-28}	1.91×10^{-26}	1.58×10^{-23}	4.31×10^{-25}	15.28

doi:10.1371/journal.pone.0124016.t002
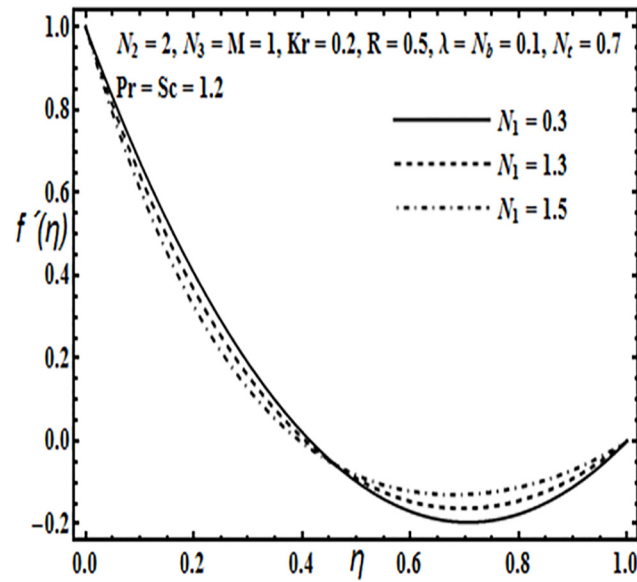
Fig 2. Effect of N_1 on $f'(\eta)$.

$$E_m^\theta = \frac{1}{k+1} \sum\nolimits_{j=0}^{k} \left\{ N_\theta \left(\sum\nolimits_{i=0}^{m} \hat{f}(\eta), \sum\nolimits_{i=0}^{m} \hat{\theta}(\eta), \sum\nolimits_{i=0}^{m} \hat{\phi}(\eta) \right)_{\eta=j\delta\eta} \right\}^2 d\eta, \tag{75}$$

$$E_m^G = \frac{1}{k+1} \sum\nolimits_{j=0}^{k} \left\{ N_G \left(\sum\nolimits_{i=0}^{m} \hat{f}(\eta), \sum\nolimits_{i=0}^{m} \hat{G}(\eta) \right)_{\eta=j\delta\eta} \right\}^2 d\eta, \tag{76}$$
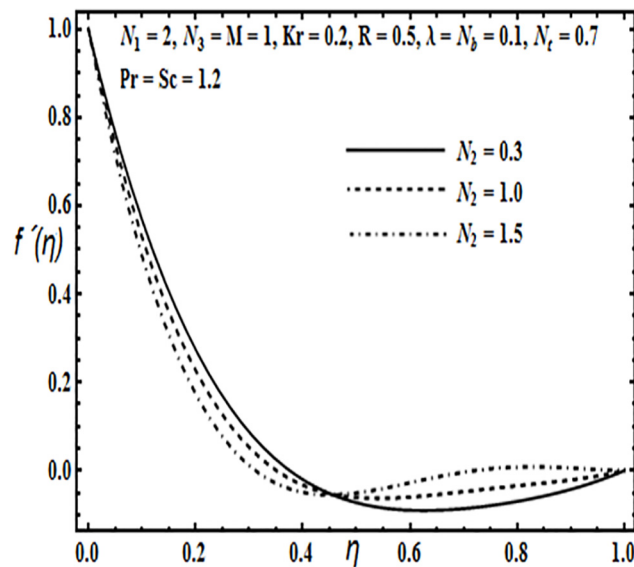
Fig 3. Effect of N_2 on $f'(\eta)$.
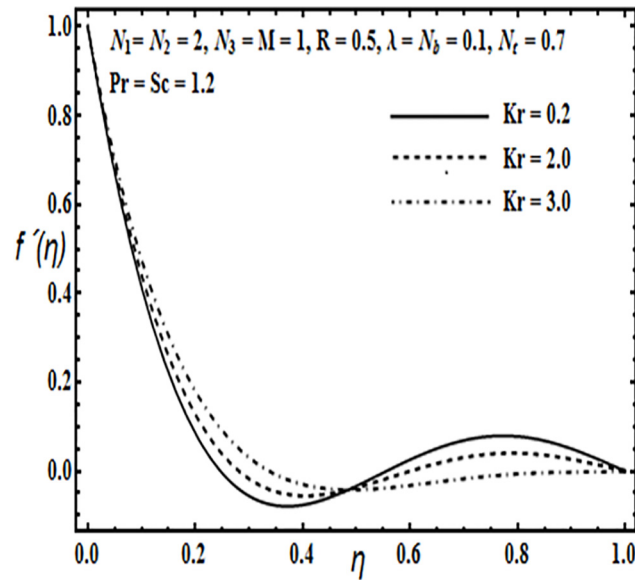
Fig 4. Effect of *Kr* on *f′(η)*.

$$E_m^\phi = \frac{1}{k+1} \sum_{j=0}^{k} \left\{ N_\phi \left(\sum_{i=0}^{m} \hat{f}(\eta), \sum_{i=0}^{m} \hat{\phi}(\eta) \right)_{\eta=j\delta\eta} \right\}^2 d\eta. \tag{77}$$

Following Liao [24]

$$E_m^t = E_m^f + E_m^g + E_m^\theta + E_m^G + E_m^\phi, \tag{78}$$
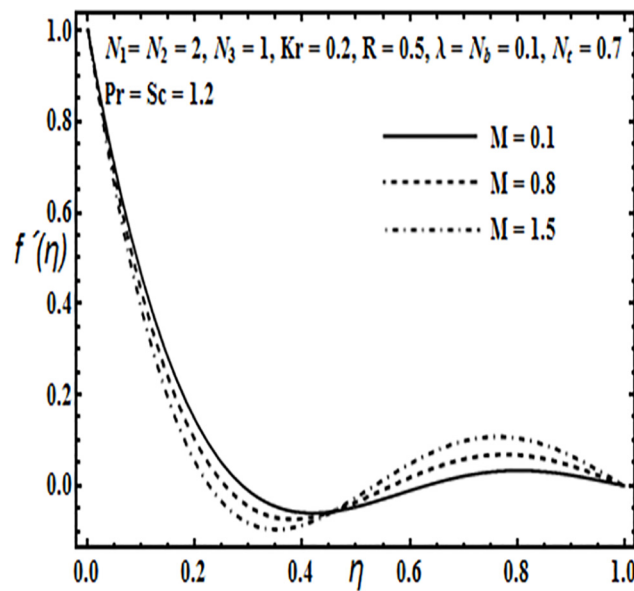
Fig 5. Effect of *M* on *f′(η)*.
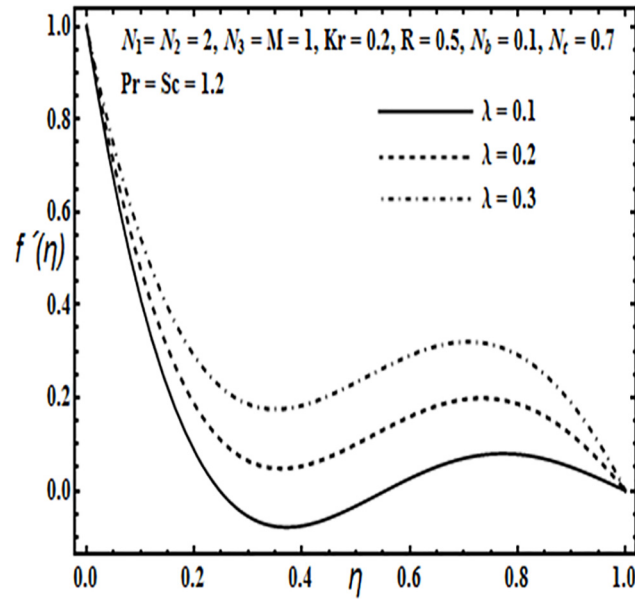
Fig 6. Effect of λ on f′(η).

where E_m^t is total averaged squared residual error, $\delta\eta = 0.5$, $k = 20$. Total and individual averaged squared residual errors are computed using $N_1 = N_2 = N_3 = 0.10$, $R = 0.20$, $n = 0.50$, $M = 0.10 = Kr = Nt = Nb = \lambda$, $Pr = 1 = Sc$. By means of computational software Mathematica we obtained the total and individual average squared residual errors at various order of iterations using highly efficient Mathematica package **BVPh2. 0** which can be found at http:// numericaltank.sjtu.edu.cn/BVPh2_0.htm. The basic idea is to **minimize** the total average squared residuals and determining the corresponding local optimal convergence control
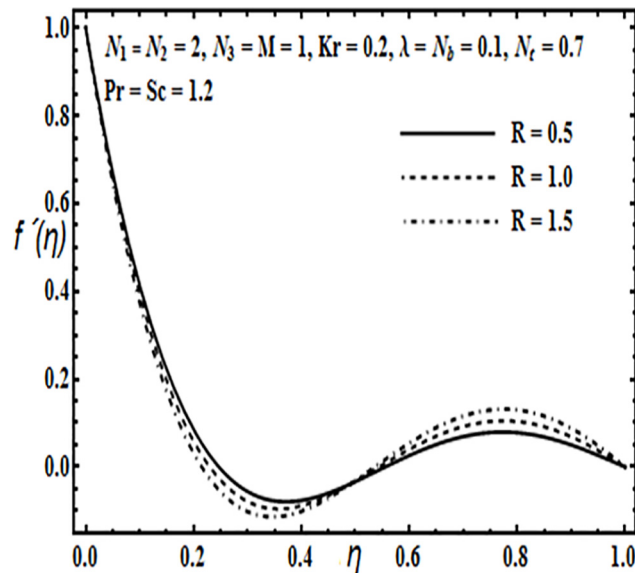
Fig 7. Effect of R on f′(η).
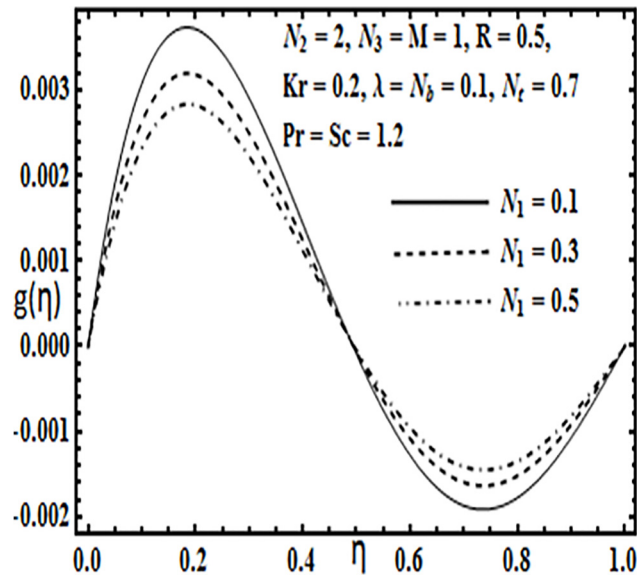
Fig 8. Effect of N_1 on $g(\eta)$.

parameters. For this purpose, Tables 1 and 2 are prepared for the case of various optimal convergence control parameters. Table 1 gives the minimum value of total averaged squared residual error at several order of iterations while Table 2 is presented for the individual average squared residual error at different orders of approximations using the optimal values from Table 1 at $m = 6$. It is quite obvious from these two tables that the averaged squared residual errors and total averaged squared residual errors continue decreasing as we increase the order of approximation. So, Optimal Homotopy Analysis Method is an extremely effective tool in obtaining convergent series solutions for highly nonlinear systems of differential equations.
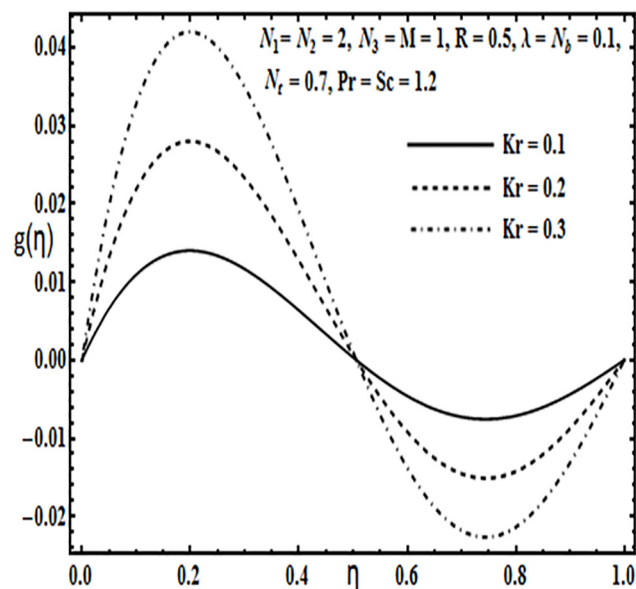

Fig 9. Effect of Kr on $g(\eta)$.
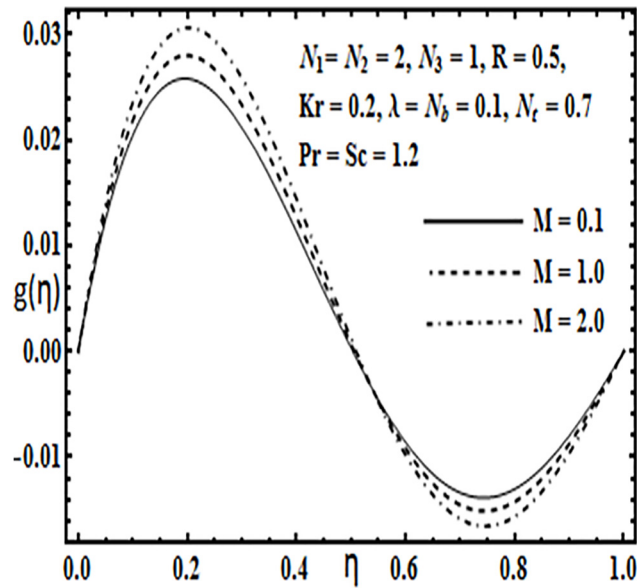
Fig 10. Effect of M on $g(\eta)$.

2. Numerical Solution

Despite OHAM, the governing system of Eqs (10)–(14) is also solved numerically using midpoint integration as a basic scheme and Richardson extrapolation as an enhancement scheme with highly efficient computational software Maple as used by several other authors [26–30] This scheme works by transforming the governing system of nonlinear higher order differential equations into a system of first order ordinary differential equations which are then solved using iterative schemes through midpoint integration as it belongs to the class of higher order
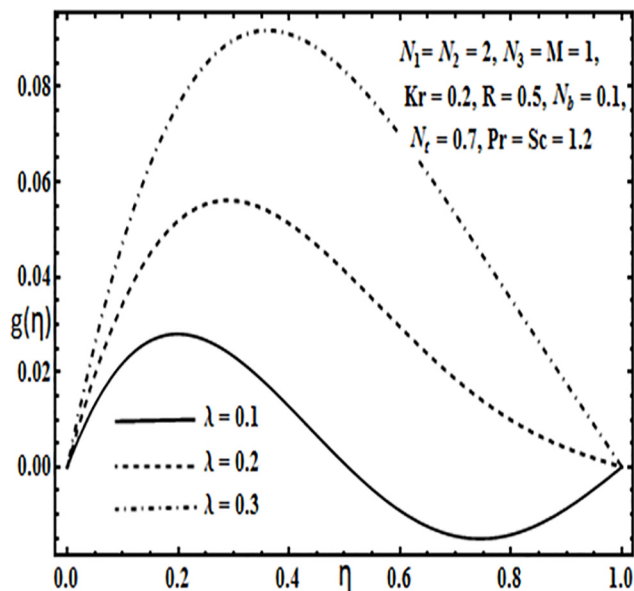

Fig 11. Effect of λ on $g(\eta)$.
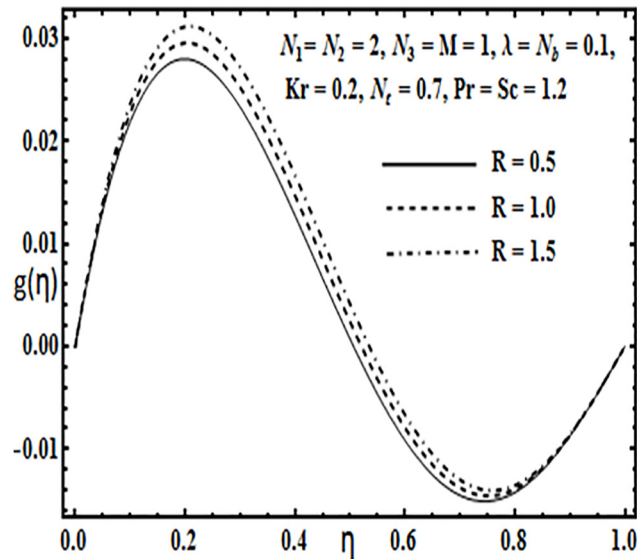
Fig 12. Effect of R on $g(\eta)$.

Runge-Kutta methods. A mesh size of $\Delta h = 0.001$ was set for a convergence criterion of 10^{-6} in our computations. Our computed numerical results are in very good agreement with analytical results obtained by optimal homotopy analysis method. We are thus confident that our applied numerical algorithm is up to the mark.

Results and Discussion

The aim here is to discuss the behavior of velocity, temperature, micro rotation and concentration profiles against emerging physical parameters in our flow problem. Figs 2–25 are plotted
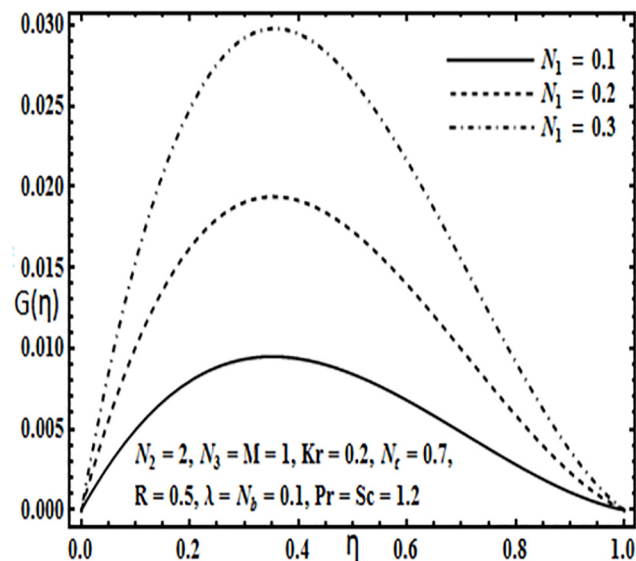

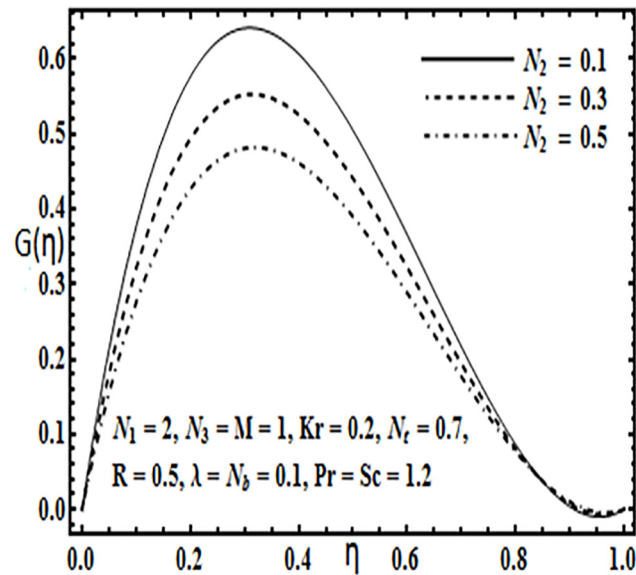**Fig 13. Effect of N_1 on $G(\eta)$.**

Fig 14. Effect of N_2 on $G(\eta)$.

doi:10.1371/journal.pone.0124016.g014

for this purpose. Figs 2–7 are plotted to determine the influence of coupling parameter N_1, spin gradient viscosity parameter N_2, rotation parameter Kr, Hartman number M, porosity parameter λ and Reynolds number R on velocity profile $f'(\eta)$. From Figs 2 and 3 we observe that the influence of coupling parameter N_1 and spin gradient viscosity parameter N_2 on the velocity profile $f'(\eta)$ is similar, i.e. it initially decreases near the lower stretching plate and from the center of the plates towards the upper plate the behavior is reversed.
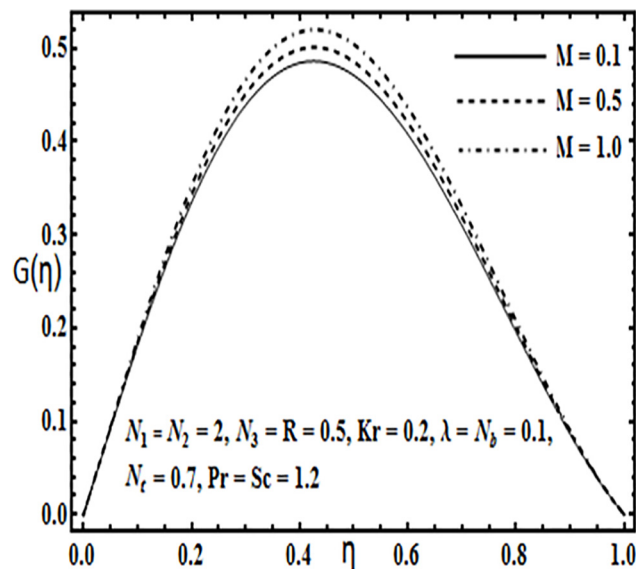

Fig 15. Effect of M on $G(\eta)$.

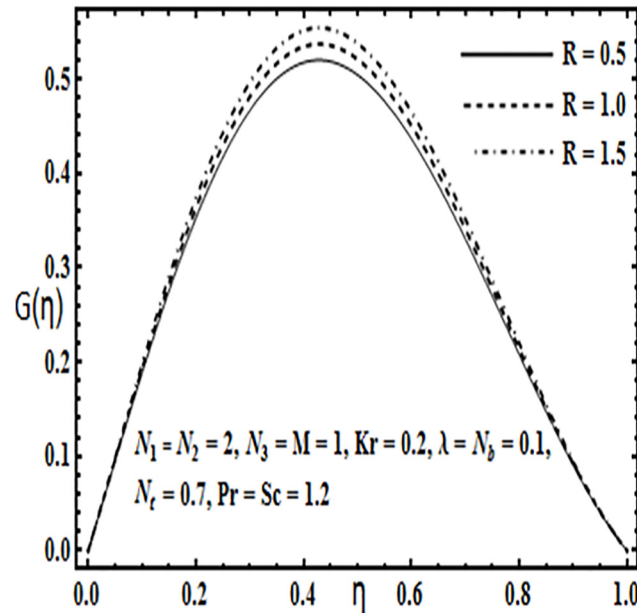doi:10.1371/journal.pone.0124016.g015

Fig 16. Effect of *R* on *G(η)*.

On the other hand, from Figs [4] and [5] velocity profile $f'(\eta)$ increases towards the main stream with an increase in rotation parameter *Kr* Hartman number *M* and then it tends to decrease towards the upper plate.

The effects of porosity parameter λ and Reynolds number *R* are revealed through Figs [6] and [7]. From [Fig 6] we observe that increasing the porosity parameter λ results in an increase in the velocity profile $f'(\eta)$ from lower towards the upper plate. From [Fig 7] velocity profile $f'(\eta)$ decreases near the lower plate but increases towards the upper plate.
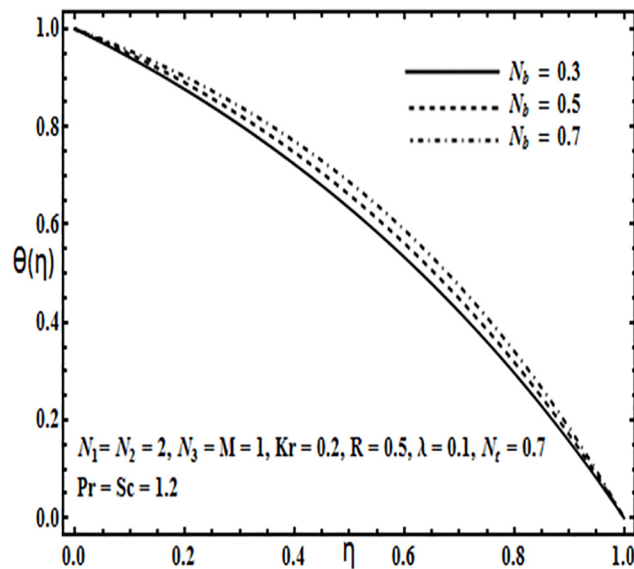

Fig 17. Effect of N_b on *θ(η)*.
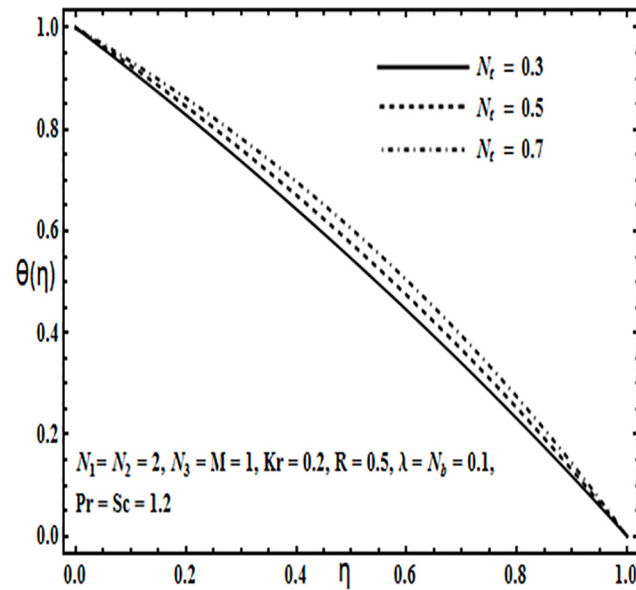
Fig 18. Effect of N_t on $\theta(\eta)$.

The impact of embedding physical parameters such as coupling parameter N_1, rotation parameter Kr, Hartman number M, porosity parameter λ and Reynolds number R on transverse velocity $g(\eta)$ is displayed through Figs 8–12. Figs 8 and 9 depict that coupling parameter N_1 and rotation parameter Kr have opposite influence on transverse velocity $g(\eta)$. Similarly from Fig 10 increasing the magnetic field through Hartman number M increases the transverse velocity $g(\eta)$ near the lower plate but contrary behavior is observed near the upper plate. It is quite evident from Figs 11 and 12 that increasing the porosity parameter λ and Reynolds number R have a positive influence on the transverse velocity $g(\eta)$.
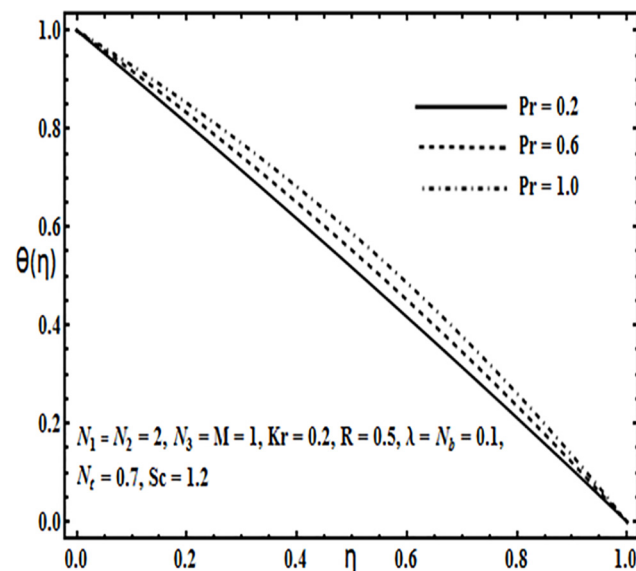

Fig 19. Effect of Pr on $\theta(\eta)$.
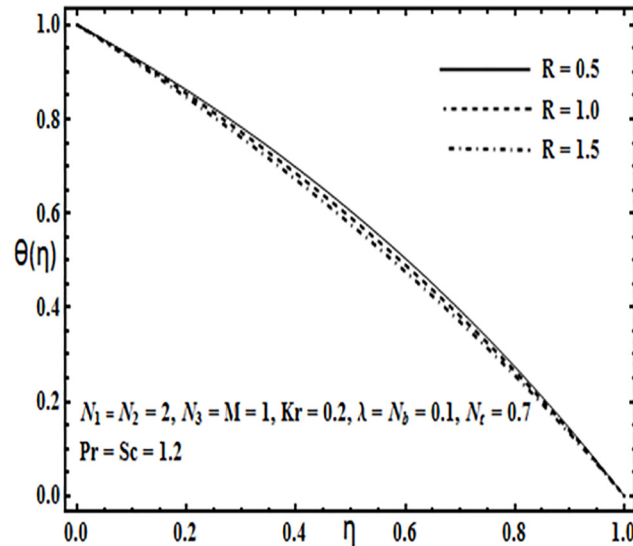
Fig 20. Effect of R on θ(η).

Variation in the micro rotation profile $G(\eta)$ against various parameters such as coupling parameter N_1, spin gradient viscosity parameter N_2, Hartman number M and Reynolds number R are presented through Figs 13–16. From Figs 13 and 14 the effects of coupling parameter N_1 and spin gradient viscosity parameter N_2 on the micro rotation profile $G(\eta)$ are quite opposite to each other. From Fig 13 increasing the coupling parameter N_1 leads to an increase in the micro rotation profile $G(\eta)$ while it decreases with an increase in spin gradient viscosity parameter N_2 (See Fig 14). Influence of Hartman number M and Reynolds number R on the micro rotation profile $G(\eta)$ is found to be similar from Figs 15 and 16. Both these parameters enhance the micro ration profile $G(\eta)$ between the parallel plates.
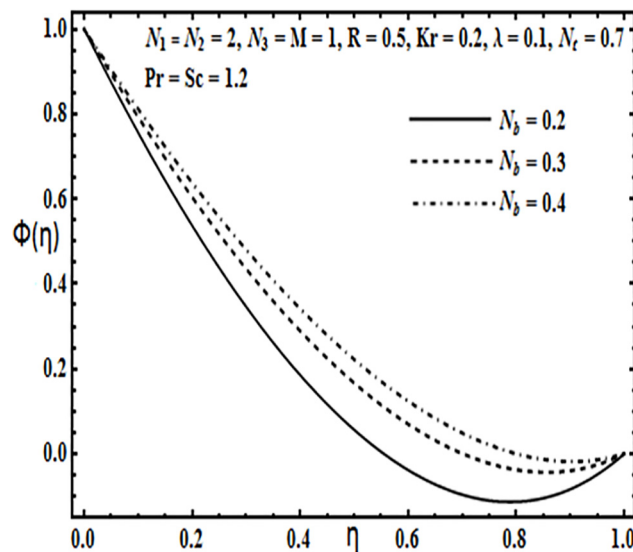
Fig 21. Effect of N_b on $\phi(\eta)$.
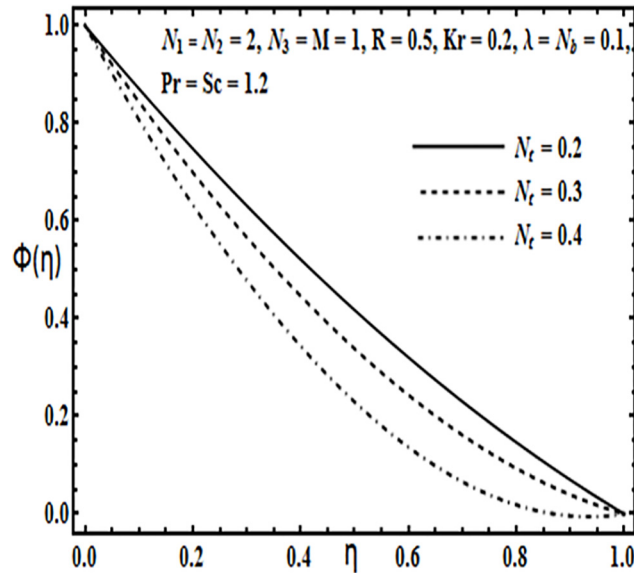
Fig 22. Effect of N_t on $\phi(\eta)$.

The impact of physical parameters such as Brownian motion parameter N_b, thermophoresis parameter N_t, Prandtl number Pr and Reynolds number R on the temperature profile $\theta(\eta)$ is presented through Figs 17–20. From Figs 17 and 18 temperature profile $\theta(\eta)$ increases significantly with an increase in Brownian motion N_b as well as thermophoresis parameter N_t. Figs 19 and 20 illustrate effects of Prandtl number Pr and Reynolds number R on the temperature profile $\theta(\eta)$. Temperature profile $\theta(\eta)$ increases with an increase in Prandtl number Pr(Fig 19), while it decreases with increasing Reynolds number R (Fig 20).
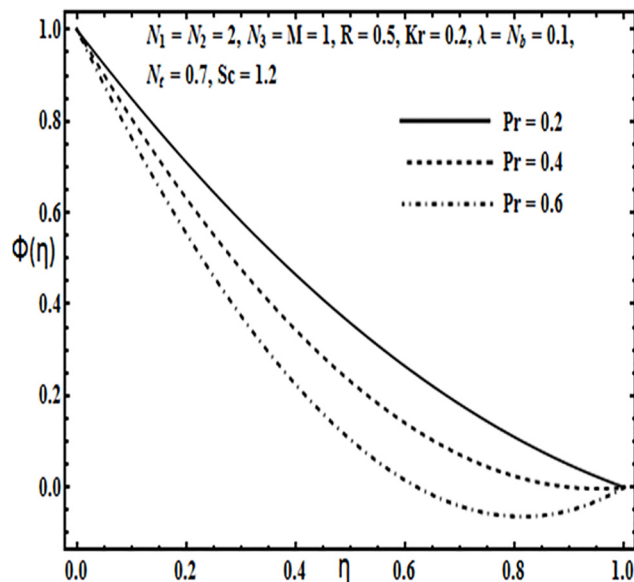
Fig 23. Effect of Pr on $\phi(\eta)$.
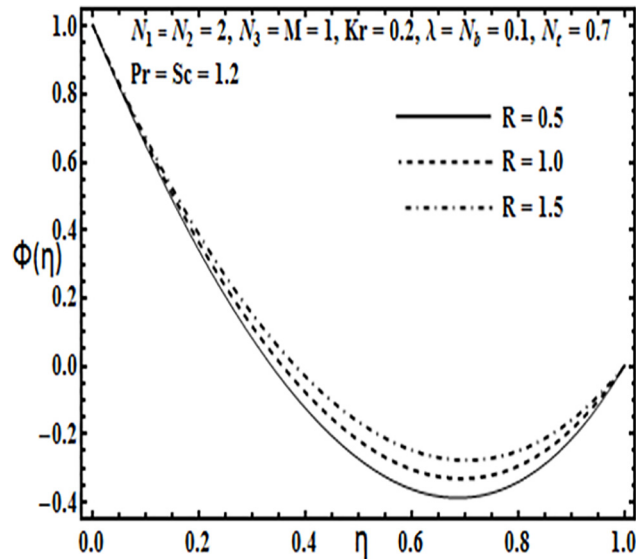
Fig 24. Effect of *R* on $\phi(\eta)$.

The effect of physical parameters such as Brownian motion parameter N_b, thermophoresis parameter N_t, Prandtl number Pr, Reynolds number R and Schmidt number Sc on the concentration profile $\varphi(\eta)$ is presented through Figs 21–25. Figs 21 and 22 indicate that Brownian motion parameter N_b increases while thermophoresis parameter N_t decreases the concentration profile $\varphi(\eta)$ between the plates. From Figs 23 and 24 concentration profile $\varphi(\eta)$ decreases with an increase in Prandtl number Pr while it increases with an increase in Reynolds number R. Finally Fig 25 shows that for large values of Schmidt number Sc, concentration profile $\varphi(\eta)$ decreases between the parallel plates.

Fig 25. Effect of *Sc* on $\phi(\eta)$.

Table 3. Numerical values of skin friction at the wall when N_2 = 1.0.

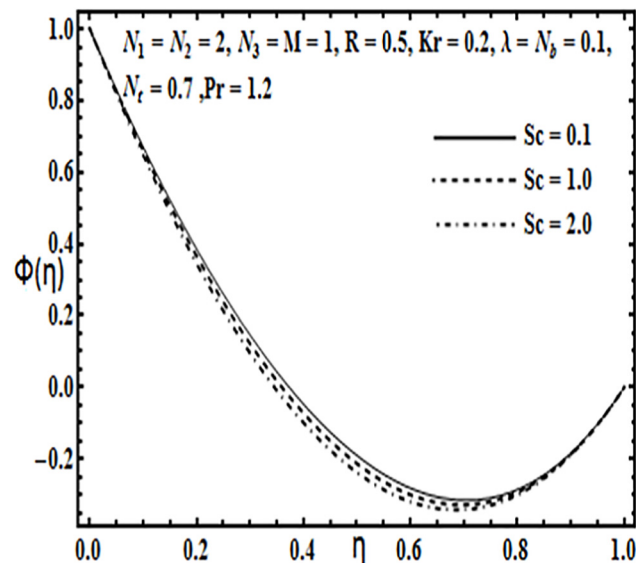| N_1	N_3	M	Kr	R	$C_f = (1 + N_1)f''(0) + N_1 G(0)$			
					n = 0.0 (Strong Concentration)		n = 0.50 (Weak Concentration)	
					Numerical	Optimal Ham	Numerical	Optimal Ham
0.0	0.1	0.1	0.1	0.5	−3.46067	−3.46067	−3.46067	−3.46067
0.1					−3.79947	−3.79947	−3.62896	−3.62896
0.5					−5.13213	−5.13213	−4.31894	−4.31894
0.1	0.0	0.1	0.1	0.5	−3.79947	−3.79947	−3.62881	−3.62881
	0.3				−3.79947	−3.79947	−3.62924	−3.62924
	0.5				−3.79947	−3.79947	−3.62953	−3.62953
0.1	0.1	0.0	0.1	0.5	−3.78723	−3.78723	−3.61727	−3.61727
		0.5			−3.84813	−3.84813	−3.67540	−3.67540
		1.0			−3.90829	−3.90829	−3.73284	−3.73284
0.1	0.1	0.1	0.0	0.5	−3.79942	−3.79942	−3.62890	−3.62890
			0.5		−3.80078	−3.80078	−3.63020	−3.63020
			1.0		−3.80486	−3.80486	−3.63410	−3.63410
0.1	0.1	0.1	0.1	0.5	−3.79947	−3.79947	−3.62896	−3.62896
				1.0	−3.84769	−3.84769	−3.67514	−3.67514
				1.5	−3.89581	−3.89581	−3.72123	−3.72123

doi:10.1371/journal.pone.0124016.t003

Physical quantities of interest such as skin friction co-efficient, Nusselt and Sherwood number are computed through Tables 3–5. Table 3 examines the influence of embedding parameters such as N_1, N_3, M, Kr and R on skin friction coefficient. All these parameters have a positive influence on skin friction at the lower plate but it is interesting to mention here that

Table 4. Numerical values of heat flux at the wall when N_2 = 1.0, N_3 = 0.1, λ = 0.1, M = 0.1, Kr = 0.1, Pr = 1.

N_1	N_b	N_t	R	Sc	$Nu = -\theta'(0)$			
					n = 0.0 (Strong Concentration)		n = 0.50 (Weak Concentration)	
					Numerical	Optimal Ham	Numerical	Optimal Ham
0.0	0.1	0.1	0.5	1.0	0.92042	0.92042	0.92042	0.92042
0.1					0.92044	0.92044	0.92043	0.92043
0.3					0.92049	0.92049	0.92043	0.92043
0.1	0.5	0.1	0.5	1.0	0.71075	0.71075	0.71074	0.71074
	0.8				0.57831	0.57831	0.57831	0.57831
	1.2				0.43240	0.43240	0.43240	0.43240
0.1	0.1	0.5	0.5	1.0	0.71285	0.71285	0.71284	0.71284
		0.8			0.58125	0.58125	0.58124	0.58124
		1.2			0.43578	0.43578	0.43575	0.43575
0.1	0.1	0.1	0.5	1.0	0.92044	0.92044	0.92043	0.92043
			1.0		0.95655	0.95655	0.95653	0.95653
			1.5		0.99309	0.99309	0.99306	0.99306
0.1	0.1	0.1	0.5	0.5	0.92078	0.92078	0.92077	0.92077
				1.0	0.92044	0.92044	0.92043	0.92043
				1.5	0.92010	0.92010	0.92009	0.92009

doi:10.1371/journal.pone.0124016.t004

Table 5. Numerical values of Mass flux at the wall when $N_1 = N_2 = 1.0$, $N_3 = 0.1$, $\lambda = 0.1$, $M = 0.1$, $Kr = 0.1$, $Pr = 1.2$.

				$Sh = -\varphi'(0)$			
				n = 0.0 (Strong Concentration)		**n = 0.50 (Weak Concentration)**	
N_b	N_t	R	Sc	*Numerical*	*Optimal Ham*	*Numerical*	*Optimal Ham*
0.5	0.1	0.5	1.0	1.09115	1.09115	1.09058	1.09058
0.8				1.08604	1.08604	1.08571	1.08571
1.2				1.08064	1.08064	1.08030	1.08030
0.1	0.2	0.5	1.0	1.30437	1.30437	1.30476	1.30476
	0.5			2.47999	2.47999	2.48122	2.48122
	0.8			4.41360	4.41360	4.41532	4.41532
0.1	0.1	0.5	1.0	1.11270	1.11270	1.11274	1.11274
		1.0		1.10926	1.10926	1.10935	1.10935
		1.5		1.10493	1.10493	1.10509	1.10509
0.1	0.1	0.5	0.5	1.09558	1.09558	1.09580	1.09580
			1.0	1.11270	1.11270	1.11274	1.11274
			1.5	1.12995	1.12995	1.12980	1.12980

doi:10.1371/journal.pone.0124016.t005

this increasing behavior is more prominent for the case of strong concentration i.e. $n = 0.0$ when compared to the case of weak concentration $n = 0.5$. The impact of coupling parameter N_1, Brownian motion parameter N_b, thermophoresis parameter N_t, Reynolds number R and Schmidt number Sc on the Nusselt number is depicted through Table 4. For higher values of coupling parameter N_1, Nusselt number $-\theta'(0)$ tends to increase while it decreases with an increase in, Brownian motion parameter N_b, thermophoresis parameter N_t. Similarly, it is also observed that with an increase in Reynolds number R, Nusselt number $-\theta'(0)$ also increases while it decreases with an increase in Schmidt number Sc for strong $n = 0.0$ as well as weak concentration $n = 0.5$. Finally Table 5 depicts that Sherwood number $-\phi'(0)$ responds in an opposite manner against Brownian motion parameter N_b, thermophoresis parameter N_t. Moreover local mass flux $-\phi'(0)$ decreases with Reynolds number R and it increases with an increase in Schmidt number Sc for strong $n = 0.0$ as well as weak concentration $n = 0.5$.

Concluding Remarks

Hydromagnetic flow of micropolar nanofluid between two horizontal parallel plates in a rotating system has been investigated numerically as well as analytically using optimal HAM. The core outcomes of the study can be enlisted as

- The effects of coupling parameter N_1 and Hartman number M on velocity profile $f'(\eta)$ are found to be opposite compared to viscosity parameter N_2 and rotation parameter Kr.

- Influence of magnetic field M and coupling parameter N_1 on transverse velocity $g(\eta)$ are opposing each other. Moreover it is observed that increasing the porosity parameter λ leads to an increase in the transverse velocity $g(\eta)$.

- It is observed that temperature profile $\theta(\eta)$ enhances for large values of Prandtl number Pr, thermophoresis parameter Nt and Brownian motion parameter Nb for the case of strong concentration ($n = 0$).

- Micro rotation profile $G(\eta)$ raises with coupling parameter N_1, magnetic field parameter M and Reynolds number R for strong concentration i.e. when $n = 0$.

- Increasing the thermophoresis parameter Nt and Brownian motion parameter Nb results in a contrary behavior on concentration profile $\phi(\eta)$.

- Skin friction at the lower plate tends to increase with magnetic field parameter M, rotation parameter Kr and Reynolds number R. This behavior is found to be more prominent for the case of strong concentration i.e. ($n = 0$) compared to the weak concentration ($n = 0.5$).

- Heat flux $-\theta'(0)$ at the lower plate drops with Increasing thermophoresis parameter Nt and Brownian motion parameter Nb while on the other hand mass flux $-\phi'(0)$ responds in an opposite manner against these two parameters.

Author Contributions

Analyzed the data: SN SM RM MAS. Contributed reagents/materials/analysis tools: SN SM RM. Wrote the paper: SN SM RM.

References

1. Eringen AC. Simple micropolar fluids, Int. J. Eng. Sci. 1964; 2: 205–217.

2. Eringen AC. Theory of micropolar fluids, J. Math. Mech. 1966; 16: 1–18.

3. Eringen AC. Microcontinum field theories. II. Fluent media. New York: Springer; 2001.

4. Lukaszewicz G. Micropolar fluids: Theory and applications. Basel: Brikhauser; 1999.

5. Bhargava R, Kumar L, Takhar HS. Finite element solution of mixed convection micropolar flow driven by a porous stretching sheet. Int. J. Eng. Sci. 2003; 41: 2161–2178.

6. Bhargava R, Kumar L, Takhar HS. Numerical solution of free convection MHD micropolar fluid flow between two parallel porous vertical plates. Int. J. Eng. Sci. 2003; 41: 123–136.

7. Nazar R, Amin N, Filip D, Pop I. Stagnation point flow of a micropolar fluid towards a stretching sheet. Int. J. Nonlinear Mech. 2004; 39: 1227–1235.

8. Ziabakhsh Z, Domairry G. Homotopy analysis solution of micropolar flow in a porous channel with high mass transfer. Adv. Theor. Appl. Mech. 2008; 2: 79–94.

9. Ishak A, Nazar R, Pop I. Magneto hydrodynamic flow of a micropolar fluid towards a stagnation point on a vertical surface. Comput. Math. Appl. 2008; 58: 3188–3194.

10. Joneidi AA, Ganji DD, Babaelahi M. Micropolar flow in a porous channel with high mass transfer. Int. Commun. Heat Mass. 2009; 36: 1082–1088.

11. Mohamed RA, Abo—Dahab SM. Influence of chemical reaction and thermal radiation on the heat and mass transfer in MHD micropolar flow over a vertical moving porous plate in a porous medium with heat generation. Int. J. Therm. Sci. 2009; 48: 1800–1813.

12. Rosali H, Ishak A, Pop I. Micropolar fluid flow towards a stretching/shrinking sheet in a porous medium with suction. Int. Commun. Heat Mass. 2012; 39: 826–829.

13. Mehmood R, Nadeem S, Akbar NS. Non orthogonal stagnation point flow of a micropolar second grade fluid towards a stretching surface with heat transfer. J. Taiwan Instt. Chem. Eng. 2013; 44: 586–595.

14. Aman F, Ishak A, Pop I. MHD stagnation point flow of a micropolar fluid towards a vertical plate with a convective surface boundary condition. Bull. Malays. Math. Sci. Soc. 2013; 36: 865–879.

15. Satya Narayana PV, Venkateswarlu B, Venkataramana S. Effects of hall current and radiation absorption on MHD micropolar fluid in a rotating system. Ain Shams Eng. J. 2013; 4: 843–854.

16. Turkyilmazoglu M. A note on micropolar fluid flow and heat transfer over a porous shrinking sheet. Int. J. Heat Mass Transf. 2014; 72: 388–391.

17. Choi SUS. Enhancing thermal conductivity of fluids with nanoparticles Siginer D.A., Wang H.P. (Eds.), Developments and Applications of Non-Newtonian Flows. 1995; 66: ASME, New York, 99.

18. Buongiorno J. Convective transport in nano fluids. ASME J. Heat transf. 2006; 128: 240.

19. Kuznetsov AV, Nield DA. Natural convective boundary-layer flow of a nanofluid past a vertical plate. Int. J. Therm. Sci. 2010; 49: 243.

20. Nadeem S, Mehmood R, Akbar NS. Optimized analytical solution for oblique flow of a casson nano fluid with convective boundary conditions. Int. J. Therm. Sci. 2014; 78: 90–100.

21. Sheikholeslami M, Ganji DD. Heat transfer of Cu-Water nanofluid flow between parallel plates. Powder Technol. 2013; 235: 873–879.

22. Sheikholeslami M, Bandpy MG, Ellahi R, Zeeshan A. Simulation of MHD Cuo-Water nanofluid flow and convective heat transfer considering Lorentz forces. J. Magn. Magn. Mater. 2014; 369: 69–80.

23. Hatami M, Ganji DD. Heat transfer and nanofluid flow in suction and blowing process between parallel disks in presence of variable magnetic field. J. mol. liq. 2014; 190: 159–168.

24. Liao SJ. An optimal Homotopy- analysis approach for strongly nonlinear differential equations, Commun. Nonlinear Sci. Numer. Simulat. 2010; 15: 2016.

25. Liao SJ. Notes on the Homotopy analysis method: some definitions and theorems, Comm. Nonlinear Sci. Numer. Simulat.2009; 14: 983.

26. Ascher U, Mattheij R, Russell R. Numerical Solution of Boundary Value Problems for Ordinary Differential Equations. SIAM Classics Appl. Math. 1995; 13: 327.

27. Ascher U, Petzold L. Computer Methods for Ordinary Differential Equations and Differential-Algebraic Equations. SIAM Philadelphia 1998.

28. Ellahi R, Hameed M, Numerical analysis of steady flows with heat transfer, MHD and nonlinear slip effects, Int. J. Num. Meth. Heat Fluid Flow. 2012; 22: 24–38.

29. Sheikholeslami M, Ellahi R, Hassan M, Soleimani S. A study of natural convection heat transfer in a nanofluid filled enclosure with elliptic inner cylinder, Int. J. Num. Meth. Heat Fluid Flow. 2014; 24: 1906–1927.

30. Rashidi S, Dehghan M, R. Ellahi R, Riaz M, Jamal-Abad MT. Study of stream wise transverse magnetic fluid flow with heat transfer around a porous obstacle, J. Magn. Magn. Mater. 2015; 378: 128–137.

31. Sheikholeslami M, Ganji DD. Nanofluid flow and heat transfer between parallel plates considering Brownian motion using DTM, Comput. Meth. Appl. Mech. Engg. 2015; 283: 651–663.

32. Ellahi R. The effects of MHD and temperature dependent viscosity on the flow of non-Newtonian nanofluid in a pipe: analytical solutions, Appl. Math. Modell. 2013; 37: 1451–1467.

33. Sheikholeslami M, Ashorynejad HR, Ganji DD, Kolahdooz A. Investigation of Rotating MHD Viscous Flow and Heat Transfer between Stretching and Porous Surfaces Using Analytical Method, Hindawi Publishing Corporation Mathematical Problems in Engineering Volume 2011, Article ID 258734, 17 pages, doi: 10.1155/2011/258734

34. Hatami M, Ganji DD. Natural convection of sodium alginate (SA) non-Newtonian nanofluid flow between two vertical flat plates by analytical and numerical methods. Case Studies in Thermal Engineering, 2014; 2: 14–22.

35. Sheikholeslami M, Ashorynejad HR, Ganji DD, Hashim I. Investigation of the Laminar Viscous Flow in a Semi-Porous Channel in the Presence of Uniform Magnetic Field using Optimal Homotopy Asymptotic Method, Sains Malaysiana. 2012; 41: 1177–1229.

36. Sheikholeslami M, Ashorynejad HR, Ganji DD, Yildirim A. Homotopy perturbation method for three-dimensional problem of condensation film on inclined rotating disk, Scientia Iranica B. 2012; 19: 437–442

37. Sheikholeslami M, Gorji-Bandpay M, Ganji DD. Magnetic field effects on natural convection around a horizontal circular cylinder inside a square enclosure filled with nanofluid, Int. Commun. Heat Mass Transf. 2012; 39: 978–986.

38. Ahmadi AR, Zahmatkesh A, Hatami M, Ganji DD. A comprehensive analysis of the flow and heat transfer for a nanofluid over an unsteady stretching flat plate. Powder Technology. 2014; 258: 125–133.

39. Sheikholeslami M, Ganji DD, Ashorynejad HR. Investigation of squeezing unsteady nanofluid flow using ADM, Powder Technology. 2013; 239: 259–265.

40. Hatami M, Sheikholeslami M, Ganji DD. Nanofluid flow and heat transfer in an asymmetric porous channel with expanding or contracting wall. J. Mol. Liq. 2014; 195: 230–239.

41. Sheikholeslami M, Hatami M, Ganji DD. Micropolar fluid flow and heat transfer in a permeable channel using analytical method. J. Mol. Liq. 2014; 194: 30–36.